Understanding the Effect of Ultrathin AuPd Alloy Shells of Irregularly Shaped Au@AuPd Nanoparticles with High-index Facets on Enhanced Performance of Ethanol Oxidation

Cuixia Bi,[a] Cong Feng,[a] Tingting Miao,[a] Yahui Song,[a] Dayang Wang[b] and Haibing Xia[a,*]

[a] State Key Laboratory of Crystal Materials, Shandong University, Jinan, 250100, P. R. China;

[b] School of Civil, Environmental, and Chemical Engineering, RMIT University, VIC 3001, Australia

E-mail: hbxia@sdu.edu.cn

Fig. S1 High magnification TEM images (a, b and c) of the lateral facets of ISCC-Au NPs revealing the projection angle between the surface and the {100} facets.
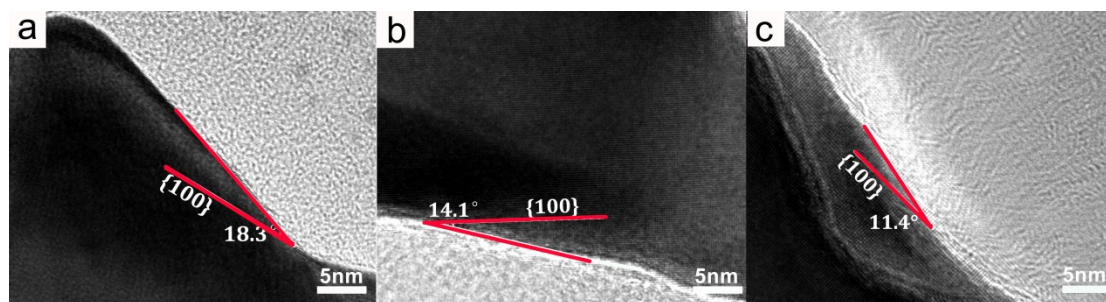
Fig. S2 TEM image of an individual HBT-Au NP (a). High magnification TEM images (b to d) of their lateral facets revealing the projection angles between the surfaces and the {111} facets. The Magnified TEM images taken from the region indicated within the boxes in (a). High magnification HRTEM images (e to g) of the edge areas of one individual HBT-Au NP (Fig. 3c in main text).
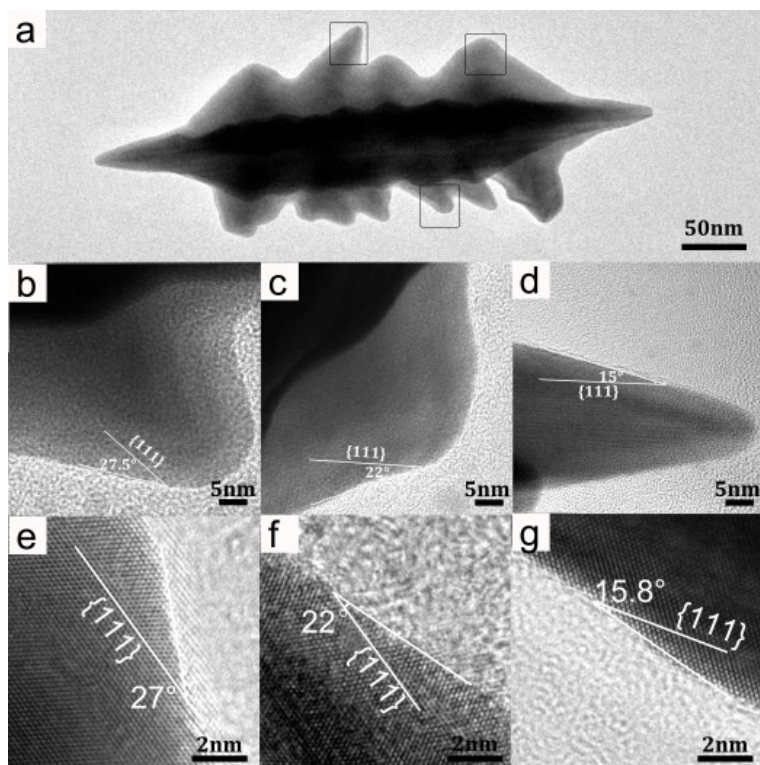
Fig. S3 TEM images (a, b and c) and normalized extinction spectra (d) of ISCC-Au NPs synthesized at different AA concentrations: 0.61 mM (a, black curve), 0.76 mM (b, red curve), and 1.51 mM (c, blue curve). The experimental details for the synthesis of ISCC-Au NPs are present in Experimental Section.
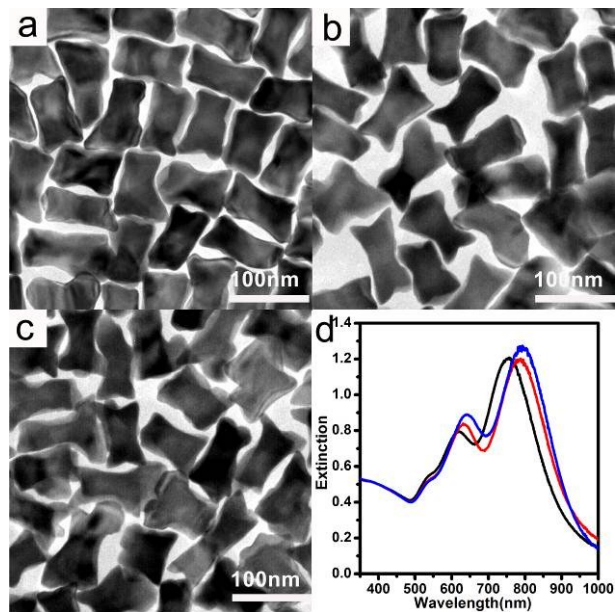
Fig. S4 CV curves of GCEs modified by the resulting ISCC-Au NPs synthesized at the AA concentration of 0.61 mM (a, black curve), 0.76 mM (b, red curve), and 1.51 mM (c, blue curve), respectively, in 0.50 M H_2SO_4 media at room temperature. The experimental details for the synthesis of ISCC-Au NPs are present in Experimental Section. The scan rate is 50 mV s^{-1}.
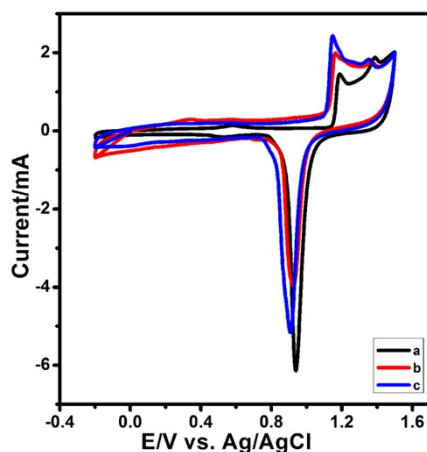
The distinct electrochemical behaviors of the Au NPs enclosed by different facets in an acidic solution were reported in a recent work.[1] The oxidation peaks of {110}-bounded Au NPs are at about 1.15 (I) and 1.23 V (II). Three oxidation peaks of {100}-bounded Au NPs are located at around 1.16 (I), 1.25 (II) and 1.34 V (III). For the {111}-bounded Au NPs, the oxidation peaks are located at around 1.15 V (I) and 1.33 V (II). As shown in Fig. S4, the CV traces of ISCC-Au NPs synthesized with AA concentration of 0.61 mM exhibit an oxidation peak around 1.15 V and 1.35V (a, black curve), while that of ISCC-Au NPs synthesized with AA concentration of 0.76 mM exhibit an oxidation peak around 1.16 V and 1.36V (b, red curve), and that of ISCC-Au NPs synthesized with AA concentration of 1.51 mM exhibit an oxidation peak around 1.19 V and 1.39V (c, blue curve).

Fig. S5 CV curves (A and B) of GCEs modified by the resulting ISCC-Au NPs synthesized with different AA concentrations in 0.30 M N_2-saturated KOH aqueous solution in the absence (A) and presence of 1.0 M methanol (B) at room temperature: 0.61 mM (a, black curve), 0.76 mM (b, red curve), and 1.51 mM (c, blue curve). The experimental details for the synthesis of ISCC-Au NPs are present in Experimental Section. The currents of (A) and (B) are normalized by the Au mass loaded on the electrodes. The peak areas are associated with the reduction of Au oxide species and are used for the evaluation of the ECSAs. The scan rate of (A) and(B) was 50 mV s^{-1} and 20 mV s^{-1}, respectively.

It is well known that Au NPs with high-index facets are expected to have high electrocatalytic performance on methanol oxidation. Here, we studied the electrocatalytic activity of ISCC-Au NPs synthesized with different concentration of AA. On the basis of the assumption that the charges associated with the reduction of oxide species are 493 mC cm^{-2} for Au surfaces, the ECSA of the ISCC-Au NPs were calculated by using CV in 0.30 M N_2-saturated KOH aqueous solution at room temperature with a scan rate of 50 mV·s^{-1}, respectively (Fig. S5A). The ECSA of the glassy carbon electrode modified by ISCC-Au NPs synthesized with different AA concentrations are 0.44, 1.19 and 1.69 m^2 g^{-1}, respectively (Table S2). These results indicate that the ISCC-Au NPs synthesized with AA concentration of 1.51 mM in the growth solution have a very large surface area and more surface defects, greatly increase the activity of the catalyst surface area.

Fig. S5B shows the electrocatalytic performance of the ISCC-Au NPs for methanol oxidation in 0.30 M N_2-saturated KOH aqueous solution containing 1.0 M methanol. The current values were normalized to Au mass loaded. The peak current density of the ISCC-Au NPs synthesized with different concentration of AA (0.61, 0.76 and 1.51 mM) are 0.68, 1.40 and 1.95 mA mg$_{Au}^{-1}$, respectively (Table S2). These results indicate that the ISCC-Au NPs synthesized with 1.51 Mm AA in the growth solution are electrochemically more accessible, which is rather important for the electrocatalytic reactions.

Fig. S6 TEM images (a, b and c) of HBT-Au NPs synthesized under different AA concentrations: 0.61 mM (a), 0.76 mM (b), and 1.51 mM (c). The experimental details for the synthesis of HBT-Au NPs are present in Experimental Section.
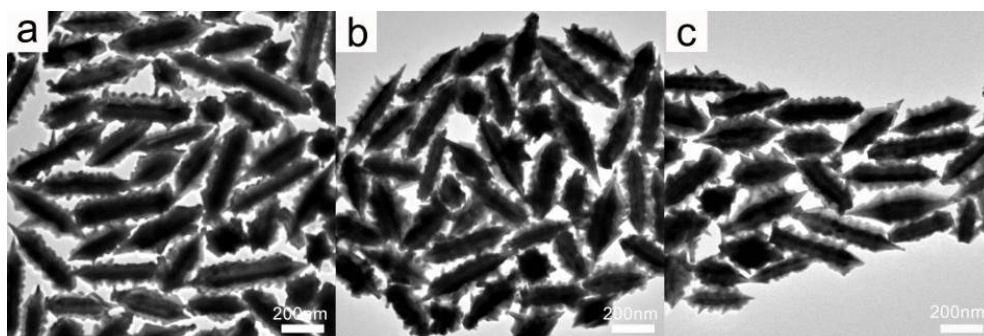
Fig. S7 CV curves of GCEs modified by the resulting HBT-Au NPs synthesized with different AA concentrations in 0.50 M H_2SO_4 media at room temperature: 0.61 mM (a, black curve), 0.76 mM (b, red curve), and 1.51 mM (c, blue curve). The experimental details for the synthesis of HBT-Au NPs are present in Experimental Section. The currents are normalized by the Au mass loaded on the electrodes. The peak areas are associated with the reduction of Au oxide species and are used for the evaluation of the ECSAs. The scan rate is 50 mV s^{-1}.
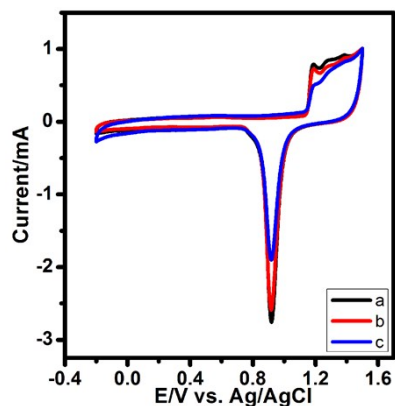
As shown in Fig. S7, as-prepared HBT-Au NPs also exhibit three distinct oxidation peaks located around 1.38 V (I), 1.27 V (II) and 1.18 V (III) respectively. Moreover, it is observed that the relative intensity of the peaks located at 1.14 V to 1.35 V in the CV of HBT-Au NPs prepared with AA concentration of 0.61 mM is higher than that in the CVs of other HBT-Au NPs prepared with AA concentration of more than 0.61 mM although their positions of oxidation peaks are rather close.

Fig. S8 CV curves (A and B) of GCEs modified by the resulting HBT-Au NPs synthesized with different AA concentrations in 0.30 M N_2-saturated KOH aqueous solution in the absence (A) and presence of 1.0 M methanol (B) at room temperature: 0.61 mM (a, black curve), 0.76 mM (b, red curve), and 1.51 mM (c, blue curve). The experimental details for the synthesis of HBT-Au NPs are present in Experimental Section. The currents of (A) and (B) are normalized by the Au mass loaded on the electrodes. The peak areas are associated with the reduction of Au oxide species and are used for the evaluation of the ECSAs. The scan rate of (A) and (B) was 50 mV s^{-1} and 20 mV s^{-1}, respectively.

Here, we also studied the electrocatalytic activity of HBT-Au NPs synthesized with different concentration of AA. The ECSA of the HBT-Au NPs were calculated by using CV in 0.30 M N_2-saturated KOH aqueous solution at room temperature with a scan rate of 50 mV·s^{-1}, respectively (Fig. S8A). The ECSA of the glassy carbon electrode modified by HBT-Au NPs synthesized with different AA concentrations are 0.60, 0.58 and 0.49 m^2 g^{-1}, respectively (Table S3). These results indicate that the HBT-Au NPs synthesized with concentration of AA is 0.61 mM in the growth solution have a very large surface area and more surface defects, greatly increase the activity of the catalyst surface area.

Fig. S8B shows the electrocatalytic performance of HBT-Au NPs for methanol oxidation in 0.30 M N_2-saturated KOH aqueous solution containing 1.0 M methanol. The current values were normalized to Au mass loaded. The peak current density of the HBT-Au NPs synthesized with different concentration of AA (0.61, 0.76 and 1.51 mM) are 1.00, 0.87 and 0.77 mA mg$_{Au}^{-1}$, respectively (Table S3). These results indicate that HBT-Au NPs synthesized with 0.61 mM AA in the growth solution are electrochemically more accessible, which is rather important for the electrocatalytic reactions.

Fig. S9 TEM images of ISCC-Au$_{99.3}$@Au$_{0.2}$Pd$_{0.5}$ NPs (a), ISCC-Au$_{98.6}$@Au$_{0.4}$Pd$_{1.0}$ NPs (b), ISCC-Au$_{97.5}$@Au$_{0.5}$Pd$_{2.0}$ NPs (c), ISCC-Au$_{96.7}$@Au$_{0.3}$Pd$_{3.0}$ NPs (d), ISCC-Au$_{96}$@Pd$_{4.0}$ NPs (e) and ISCC-Au$_{95}$@Pd$_{5.0}$ NPs (f), where the subscript numbers are the percentage of Au and Pd in the ISCC-Au$_z$@Au$_y$Pd$_x$ NPs, respectively.
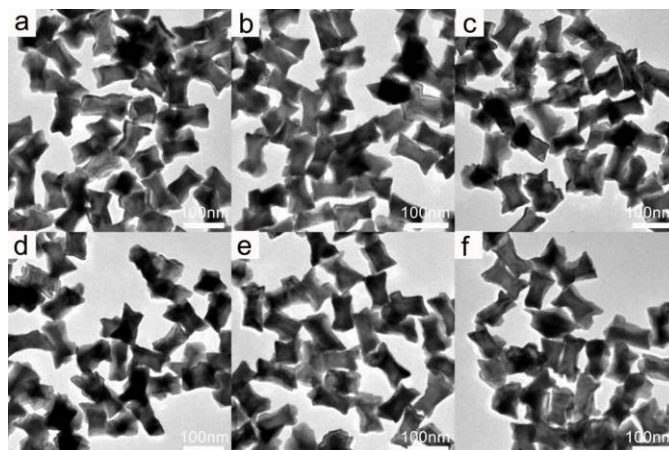
The reaction conditions for synthesis of ISCC-Au NPs as seeds were as follows. The concentrations of CTAB, HAuCl$_4$, AgNO$_3$ and AA in the reaction mixture are 95, 0.38, 0.057 and 1.51 mM, respectively. The volume of as-prepared short Au NRs solutions is 100 μL. These ISCC-Au$_z$@Au$_y$Pd$_x$ NPs are derived from corresponding ISCC-Au NPs as seeds via overgrowth of Pd on their surfaces at room temperature. The volume of as-prepared ISCC-Au NPs solutions after 4-fold concentration was 1 mL. The concentrations of Na$_2$PdCl$_4$ in (Fig. S9a to S9f) are tuned from 8.6 to 17.2, 34.4, 51.6, 68.8, and 86 μM, respectively. The concentrations of AA in (Fig. S9a to S9f) are tuned from 17.2 to 34.4, 68.8, 103.2, 137.6, and 172 μM, respectively.

Fig. S10 TEM images of HBT-$Au_{99.4}$@$Au_{0.1}Pd_{0.5}$ NPs (a), HBT-$Au_{98.9}$@$Au_{0.1}Pd_{1.0}$ (b), HBT-Au_{98}@$Pd_{2.0}$ (c), HBT-Au_{97}@$Pd_{3.0}$ (d) and HBT-Au_{95}@$Pd_{5.0}$ (e), where the subscript numbers are the percentage of Au and Pd in the HBT-Au_z@Au_yPd_x NPs, respectively.
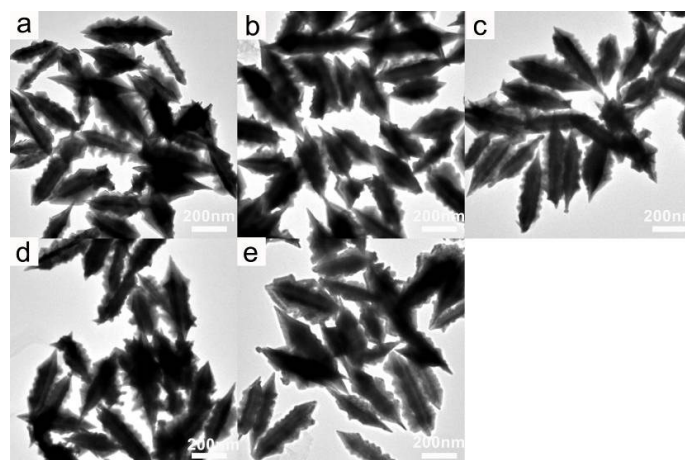
The reaction conditions for synthesis of HBT-Au NPs as seeds were as follows. The concentrations of CTAB, $HAuCl_4$, $AgNO_3$ and AA in the reaction mixture are 95, 0.38, 0.057 and 0.61 mM, respectively. The volume of as-prepared long Au NRs solutions is 160 μL. These HBT-Au_z@Au_yPd_x NPs are derived from corresponding HBT-Au NPs as seeds via overgrowth of Pd on their surfaces at room temperature. The volume of as-prepared HBT-Au NPs solutions after 5-fold concentration was 1 mL. The concentrations of Na_2PdCl_4 in (Fig. S10a to S10f) are tuned from 11.6 to 23.2, 46.2, 69.2, and 115.2 μM, respectively. The concentrations of AA in (Fig. S10a to S10f) are tuned from 23.2 to 46.4, 92.4, 138.4, and 230.4 μM, respectively.

Fig. S11 HAADF-STEM images of one individual ISCC-Au NP (a) and one individual ISCC-Au$_{97.5}$@Au$_{0.5}$Pd$_{2.0}$ NP (b).
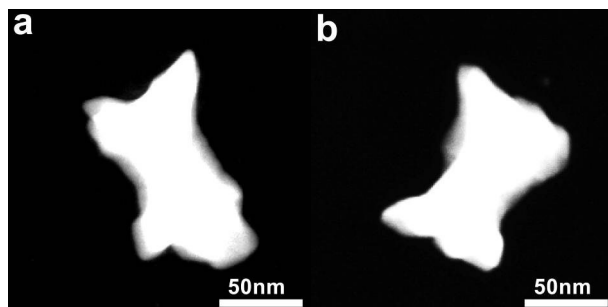
Fig. S12 HAADF-STEM images of one individual HBT-Au NP (a) and one individual $Au_{98.9}@Au_{0.1}Pd_{1.0}$ NP (b).
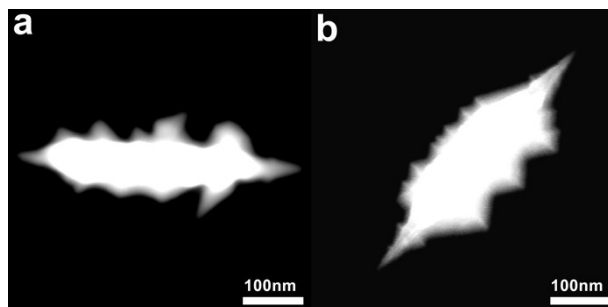
Fig. S13 UV-Vis extinction spectra of short NRs (black curve), ISCC-Au NPs (red curve) and ISCC-Au@Pd NPs (blue curve). The insets are digital pictures of the aqueous solutions of short NRs, ISCC-Au NPs and ISCC-Au@Pd NPs, respectively.
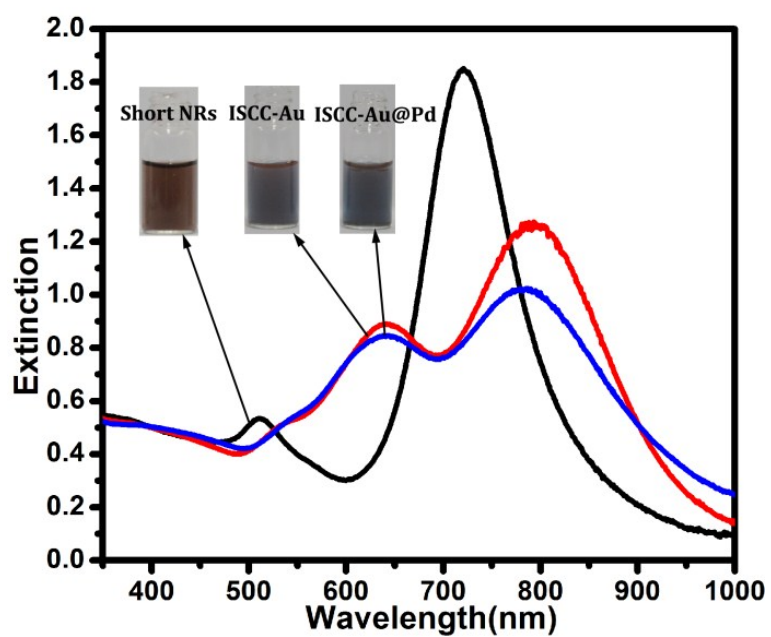
Fig. S14 UV-Vis extinction spectra of long NRs (black curve), HBT-Au NPs (red curve) and HBT-Au@Pd NPs (blue curve). The insets are digital pictures of the aqueous solutions of long NRs, HBT-Au NPs and HBT-Au@Pd NPs, respectively.
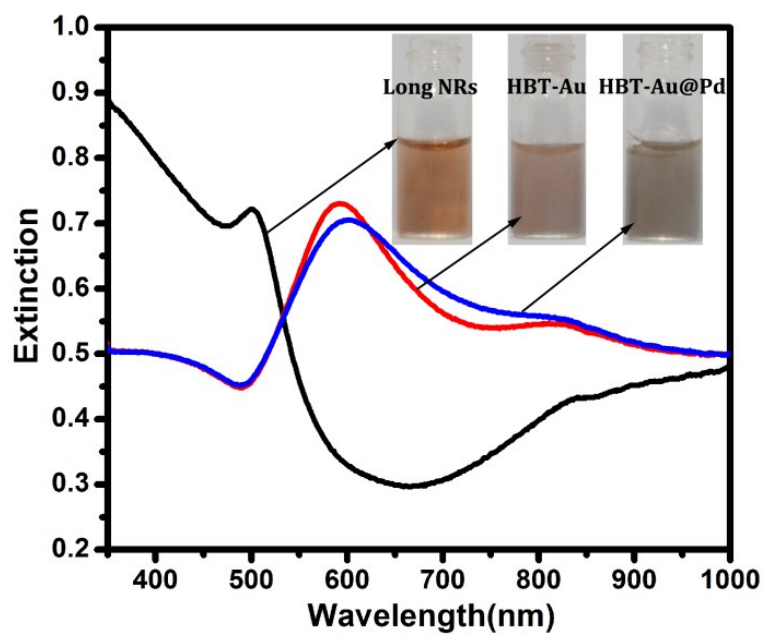
Fig. S15 TEM image (a) of a single ISCC-$Au_{97.5}$@$Au_{0.5}Pd_{2.0}$ NP and HRTEM image (b) recorded from the boxed area of (a), viewed along the $\langle 001 \rangle$ direction. The inset in (b) is the corresponding FFT image.
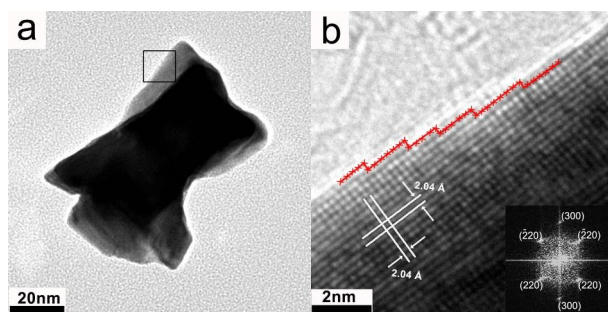
Fig. S16 TEM image (a) of a single HBT-$Au_{98.9}$@$Au_{0.1}Pd_{1.0}$ NP and HRTEM image (b) recorded from the boxed area of (a), viewed along the $\langle 011 \rangle$ direction. The inset in (b) is the corresponding FFT image.
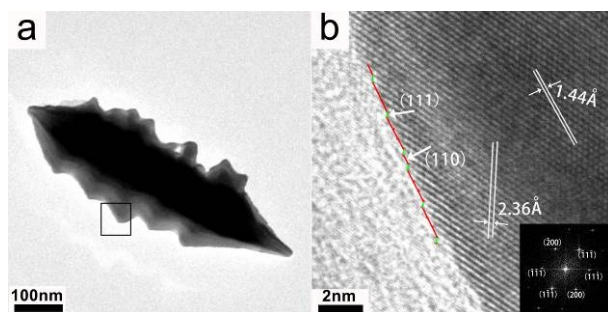
Fig. S17 CV curves (A to D) of the GCE modified by HBT-$Au_{99.4}$@$Au_{0.1}Pd_{0.5}$ NPs (a, black curve), HBT-$Au_{98.9}$@$Au_{0.1}Pd_{1.0}$ NPs (b, red curve), HBT-$Au_{98.0}$@$Pd_{2.0}$ NPs (c, blue curve), HBT-$Au_{97.0}$@$Pd_{3.0}$ NPs (d, cyan curve) and HBT-Au_{95}@$Pd_{5.0}$ NPs (e, magenta curve) in 0.30 M N_2-saturated KOH aqueous solution in the absence (A and B) and presence of 0.50 M ethanol (C and D) at room temperature. The currents of (A and C) and (B and D) were normalized by the Pd mass loaded on GCE and the ECSA values, respectively. The scan rate of (A and B) and (C and D) are 50 mV s^{-1} and 20 mV s^{-1}, respectively.
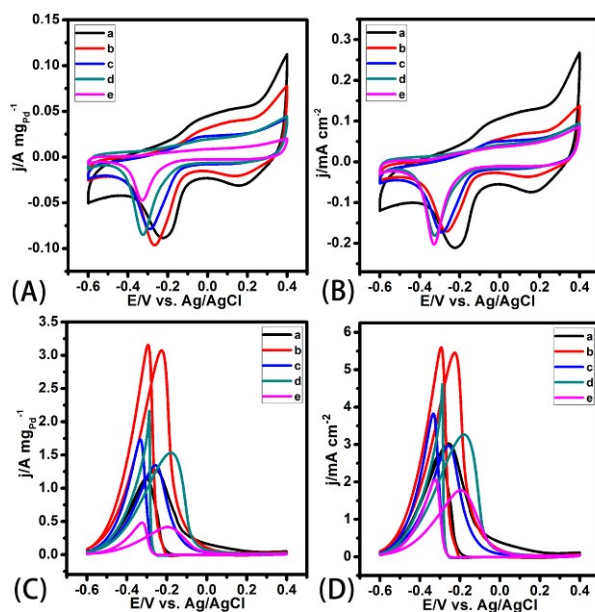
Fig. S18 XRD patterns of as-prepared ISCC-$Au_{97.5}@Au_{0.5}Pd_{2.0}$ NPs (a) and HBT-$Au_{98.9}@Au_{0.1}Pd_{1.0}$ NPs (b).
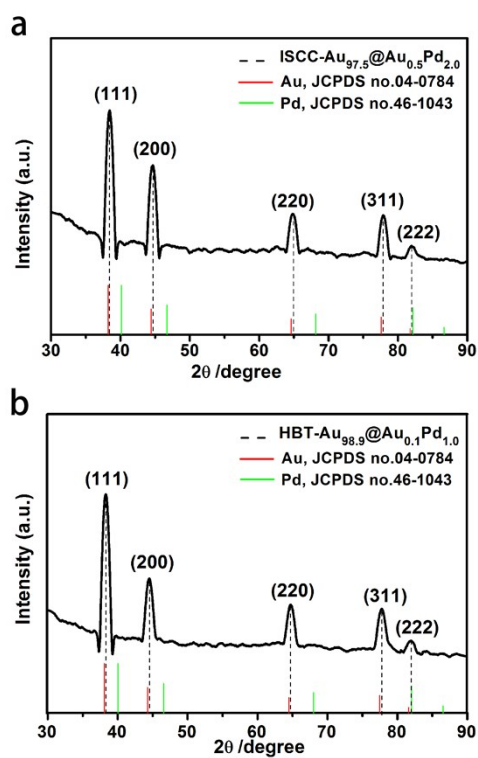
Fig. S19 CV curves (A and B) of GCE modified by (a) ISCC-$Au_{97.5}@Au_{0.5}Pd_{2.0}$ NPs, (b) HBT-$Au_{98.9}@Au_{0.1}Pd_{1.0}$ NPs and (c) commercial Pd/C catalysts in 0.30 M N_2-saturated KOH aqueous solution at room temperature. The currents of (A) and (B) were normalized by the Pd mass loaded and the ECSA values, respectively. The scan rate of (A) and (B) is 50 mV s^{-1}.
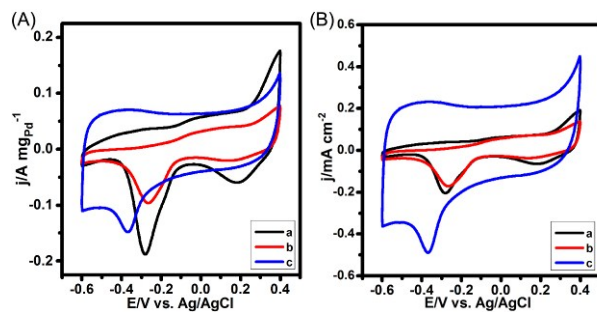
Fig. S20 XPS spectra of Au 4f signals of ISCC-Au NPs, ISCC-$Au_{97.5}$@$Au_{0.5}Pd_{2.0}$ NPs and HBT-$Au_{98.9}$@$Au_{0.1}Pd_{1.0}$ NPs.
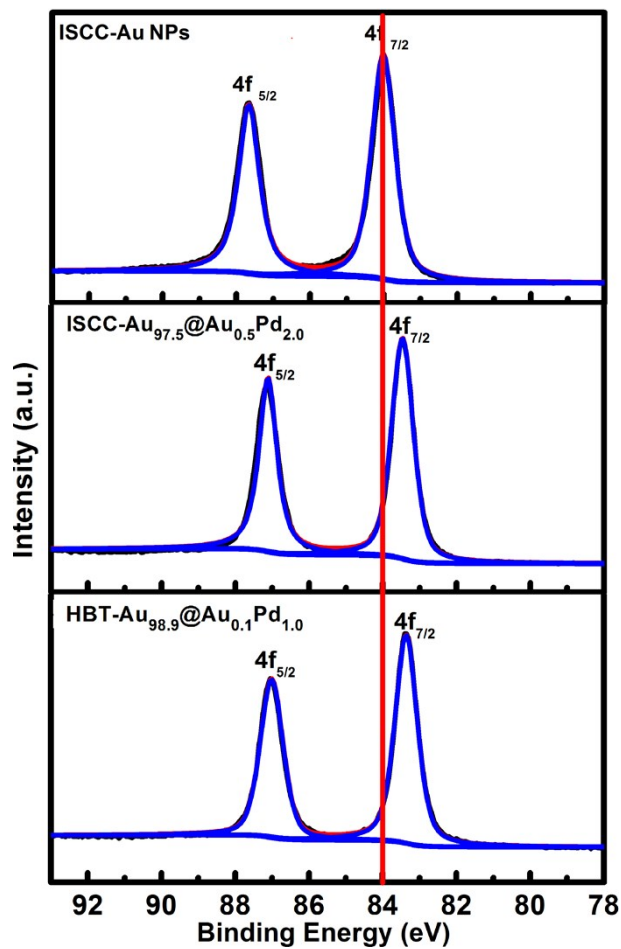
Table S1. Amount of Pd precursors used for synthesis alloyed or core-shell Au-Pd NPs.

Shape	amount of Pd precursors used for synthesis
trisoctahedral Au@Pd NPs[2]	20%
tetrahexahedral and hexoctahedral Au@Pd NPs[2]	33%
trisoctahedral and tetrahexahedral Au@Pd NPs[3]	22%
convex Au@Pd NPs[4]	27%
highly branched concave Au/Pd bimetallic NPs[5]	40%

Table S2. Projection angles between {100} and {*hk0*} facets.

{hk0}	Angle with {100}
{110}	45°
{210}	26.6°
{310}	18.4°
{410}	14°
{510}	11.4°
{710}	8.1°

Table S3. Projection angles between {111} and {hhl} facets.

{hhl}	Angle with {111}
{221}	15.8°
{331}	22.0°
{441}	25.3°
{551}	27.2°
{661}	28.5°
{771}	29.5°
{881}	30.2°
{991}	30.8°

Table S4. Summary of ECSAs and mass-normalized current density of GCE modified by ISCC-Au NPs synthesized with different AA concentrations in 0.30 M N_2-saturated KOH aqueous solution in the absence and presence of 1.0 M methanol at room temperature.

AA (mM)	ECSA [m^2 g^{-1}]	Mass activity [mA mg^{-1}]
0.61	0.44	0.68
0.76	1.19	1.40
1.51	1.69	1.95

The ECSAs of ISCC-Au NPs catalysts were estimated by the following equation, respectively:

$$ECSA = Q_o/q_o$$

where Q_o is the surface charge that can be obtained via integrating from the area under the CV trace of oxygen desorption (-0.1 ~ 0.3 V), and q_o is the charge required for desorption of monolayer of oxygen on the Au surface (493 $\mu C/cm^2$).[6]

Table S5. Summary of ECSAs and mass-normalized current density of GCE modified by HBT-Au NPs synthesized with different AA concentrations in 0.30 M N_2-saturated KOH aqueous solution in the absence and presence of 1.0 M methanol at room temperature.

AA (mM)	ECSA [m^2 g^{-1}]	Mass activity [mA mg^{-1}]
0.61	0.60	1.00
0.76	0.58	0.87
1.51	0.49	0.77

Table S6. Summary of the total and surface compositions of HBT-Au_z@Au_yPd_x NPs obtained by EDS and CV curves. The molar ratio of AA-to-Pd^{2+} is 2.

Sample	Pd^{2+} (μM)	Molar ratio of Pd-to-Au (%)	total content		surface composition			
			Au (at%)	Pd (at%)	Au (at%)	Pd (at%)	1-m (Au%)	m (Pd%)
HBT-$Au_{99.4}$@$Au_{0.1}Pd_{0.5}$ NPs	11.6	0.5	99.5	0.5	0.1	0.5	16.7	83.3
HBT-$Au_{98.9}$@$Au_{0.1}Pd_{1.0}$ NPs	23.2	1.0	99.0	1.0	0.1	1.0	9.0	91.0
HBT-$Au_{98.0}$@$Pd_{2.0}$ NPs	46.2	2.0	98.0	2.0	0	2.0	0	100
HBT-$Au_{97.0}$@$Pd_{3.0}$ NPs	69.2	3.0	97.0	3.0	0	3.0	0	100
HBT-$Au_{95.0}$@$Pd_{5.0}$ NPs	115.2	5.0	95.0	5.0	0	5.0	0	100

Table S7. Summary of ECSAs, current density normalized by mass and current density normalized by ECSA of GCE modified by ISCC-Au$_{99.3}$@Au$_{0.2}$Pd$_{0.5}$ NPs, ISCC-Au$_{98.6}$@Au$_{0.4}$Pd$_{1.0}$ NPs, ISCC-Au$_{97.5}$@Au$_{0.5}$Pd$_{2.0}$ NPs, ISCC-Au$_{96.7}$@Au$_{0.3}$Pd$_{3.0}$ NPs, ISCC-Au$_{96.0}$@Pd$_{4.0}$ NPs and ISCC-Au$_{95.0}$@Pd$_{5.0}$ NPs as catalysts on ethanol oxidation in 0.30 M KOH solution containing 0.50 M ethanol, respectively.

Pd-to-Au molar ratio	ECSA [m^2 g^{-1}]	Mass activity [A mg^{-1}]	Specific activity [mA cm^{-2}]
0.005	112.08	1.60	1.41
0.01	120.96	3.29	2.72
0.02	92.11	4.15	4.51
0.03	95.81	3.64	3.82
0.04	91.73	2.04	2.21
0.05	82.93	1.32	1.62

The ECSAs of ISCC-Au@AuPd NPs NPs catalysts were estimated by the following equation, respectively:

$$ECSA = Q_o/q_o$$

where Q_o is the surface charge that can be obtained via integrating from the area under the CV trace of oxygen desorption (-0.5 ~ -0.2 V), and q_o is the charge required for desorption of monolayer of oxygen on the Au-Pd surface (430 μC/cm^2).[7]

Table S8. Summary of ECSAs, current density normalized by mass and current density normalized by ECSA of GCE modified by HBT-Au$_{99.4}$@Au$_{0.1}$Pd$_{0.5}$ NPs, HBT-Au$_{98.9}$@Au$_{0.1}$Pd$_{1.0}$ NPs, HBT-Au$_{98}$@Pd$_{2.0}$ NPs, HBT-Au$_{97.0}$@Pd$_{3.0}$ NPs and HBT-Au$_{95.0}$@Pd$_{5.0}$ NPs as catalysts on ethanol oxidation in 0.30 M KOH solution containing 0.50 M ethanol, respectively.

Pd-to-Au molar ratio	ECSA [m^2 g^{-1}]	Mass activity [A mg^{-1}]	Specific activity [mA cm^{-2}]
0.005	41.95	1.27	3.03
0.01	56.39	3.07	5.45
0.02	45.27	1.34	2.97
0.03	46.96	1.54	3.26
0.05	23.38	0.41	1.77

Table S9. XPS shifts for the Au 4f signals for ISCC-Au NPs, ISCC-Au$_{97.5}$@Au$_{0.5}$Pd$_{2.0}$ NPs and HBT-Au$_{98.9}$@Au$_{0.1}$Pd$_{1.0}$ NPs.

	Au 4f$_{7/2}$ peak (eV)	Au 4f$_{5/2}$ peak (eV)	ΔAu4f$_{7/2}$ (eV)
ISCC-Au NPs	83.8	87.4	0
ISCC-Au$_{97.5}$@Au$_{0.5}$Pd$_{2.0}$ NPs	83.5	87.1	-0.3
HBT-Au$_{98.9}$@Au$_{0.1}$Pd$_{1.0}$ NPs	83.4	87.0	-0.4

References

(1) J. F. Wang, J. X. Gong, Y. S. Xiong, J. D. Yang, Y. Gao, Y. L. Liu, X. Q. Lu and Z. Y. Tang, *Chem. Commun.,* 2011, **47**, 6894-6896.

(2) Y. Yu, Q. B. Zhang, B. Liu and J. Y. Lee, *J. Am. Chem. Soc.,* 2010, **132**,18258-18265.

(3) F. Wang, C. H. Li, L. D. Sun, H. S. Wu, T. Ming, J. F. Wang, J. C. Yu and C. H. Yan, *J. Am. Chem. Soc.*, 2011, **133**, 1106-1111.

(4) D. Kim, Y. W. Lee, S. B. Lee and S. W. Han, *Angew. Chem., Int. Ed.*, 2012, **51**, 159-163.

(5) L. F. Zhang, S. L. Zhong and A. W. Xu, *Angew. Chem., Int. Ed.*, 2013, **52**, 645-649.

(6) A. Habrioux, W. Vogel, M. Guinel, L. Guetaz, K. Servat, B. Kokoh and N. Alonso-Vante, *Phys. Chem. Chem. Phys.*, 2009, **11**, 3573-3579.

(7) L. Xiao, L. Zhuang, Y. Liu, J. T. Lu and H. D. Abruna, *J. Am. Chem. Soc.,* 2009, **131**, 602-608.